J. Fluid Mech. (2025), *vol.* 1006, A4, doi:10.1017/jfm.2025.16

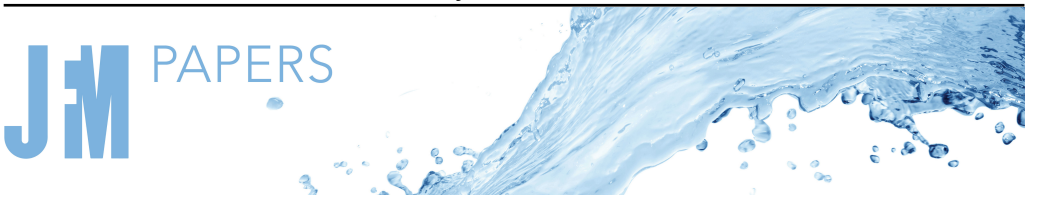

Faraday waves and period tripling in a horizontal circular tank

Stuart William Colville[1], **Y.-M. Scolan**[2], **Francesco Gambioli**[3], **Deborah Greaves**[1], **Edward Ransley**[1] **and Yeaw Chu Lee**[1]

[1]School of Engineering, Computing and Mathematics, University of Plymouth, Drake Circus, Plymouth PL4 8AA, UK

[2]ENSTA IPP - IRDL UMR 6027, 2 Rue François Verny, 29200 Brest, France

[3]Airbus Loads & Aeroelastics Dept., Airbus, Pegasus House, Aerospace Ave., Filton, Bristol BS34 7PA, UK

Corresponding author: Stuart William Colville, stuart.colville@plymouth.ac.uk

(Received 12 September 2024; revised 17 December 2024; accepted 2 January 2025)

Understanding wave kinematics is crucial for analysing the thermodynamic effects of sloshing, which can lead to pressure drops in non-isothermal cryogenic fuel tanks. In the research reported here, Faraday waves in a horizontal circular tank (partially filled with water) under vertical excitation are investigated. The tank geometry is referred to as a horizontal circular tank throughout, with its circular face oriented perpendicular to the horizontal plane. Firstly, this paper addresses the eigenvalue problem through linear potential flow theory, in order to provide theoretical evidence of Faraday waves in horizontal circular tanks, the impact the density ratio has on the eigenvalues is then considered. Secondly, an experimental investigation testing multiple liquid fill levels is conducted. A soft-spring nonlinear response is demonstrated throughout the parameter space. The results showed larger sloshing amplitudes for low fill levels and smaller sloshing amplitudes for high fill levels. Asymmetry between anti-nodes at the container sidewalls and through the tank centreline are evident for low fill levels. Moreover, the sloshing wave amplitude at which breaking waves occur is smaller for high fill level conditions. Finally, period tripling was observed for all fill levels tested, confirming nonlinear mode interactions before the onset to wave breaking.

Key words: wave breaking, Faraday waves, parametric instability

1. Introduction

An alternative fuel for next generation aircraft is liquid hydrogen (LH2), this requires storage at cryogenic temperatures due to its low boiling point of –253 °C. This study investigates a common problem in cryogenic fuel tanks which relates to liquid sloshing. Liquid sloshing is the free surface motion in a partially filled container under excitation. Liquid hydrogen sloshing experiments have previously demonstrated that large unstable sloshing amplitudes (near resonance) can initiate rapid pressure drops in the ullage space (Moran *et al.* 1994). The interaction between the gas and liquid phases, during sloshing, disrupts the initial thermal stratification between the two phases. This leads to heat and mass transfer from the gas phase to the liquid phase which results in ullage pressure drop. Consequently, this can cause problems with fuel delivery from the fuel tank to the gas turbine combustion chamber.

Over the last 20 years, a range of non-isothermal sloshing experiments have been conducted in upright cylinders, to investigate the pressure drop phenomena in non-isothermal conditions (Arndt *et al.* 2008; Lacapere, Vieille & Legrand 2009; Das & Hopfinger 2009; Hopfinger & Das 2009; Arndt 2012; Ludwig, Dreyer & Hopfinger 2013; Marques *et al.* 2023). This has primarily been of interest to the space industry, where LH2 is a common fuel. The studies have focused on exciting fundamental sloshing modes of the upright cylinder, and are complemented by theoretical work on the fluid stability for this geometry, which is crucial for the definition of sloshing conditions in the non-isothermal tests discussed herein (Miles 1984).

Experiments with single species liquid nitrogen (LN2) showed destratification of the interface thermal gradient during sloshing and a corresponding pressure drop in the ullage space (Lacapere *et al.* 2009). A separate sloshing test with liquid nitrogen investigated the effect of the initial ullage pressure on the sloshing induced pressure drop (Arndt *et al.* 2008). Their results showed higher initial ullage pressures, and subsequently larger thermal gradients at the interface resulted in larger pressure drops, while the time taken for the ullage to reach its minimum pressure (saturation temperature) was longer for larger initial pressures. Liquid nitrogen was also used to investigate the effect the sloshing wave height has on the pressure drop (Ludwig *et al.* 2013), and a sloshing-based Reynolds number was proposed. This determines the critical wave amplitude at which sloshing initiates heat transfer across the interface and thus initiates a pressure drop. Large pressure drops were displayed for wave breaking conditions, due to enhanced mixing between the phases. Further quantification of how different types of breaking waves effect the pressure drop has not been completed.

Very few non-isothermal studies have investigated the effect different tank fill levels have on pressure drop. Seminal work quantifying the LH2 pressure drop induced by sloshing (Moran *et al.* 1994) highlighted the sensitivity of the ullage pressure to heat and mass transfer for low ullage volumes. This work also reported a failure to find a relationship between ullage volume and pressure response for high-amplitude sloshing. In the case of low-amplitude sloshing, the relationship between these parameters was directly proportional. To the best of the authors' knowledge no experimental campaign has addressed this.

Due to the high volumetric energy density of LH2, the typical shape and location of fuel tanks for a LH2 powered aircraft will be different from current aircraft. A horizontally orientated cylindrical fuel tank located within the aircraft fuselage is a potential fuel tank geometry (Silberhorn *et al.* 2019; Onorato, Proesmans & Hoogreef 2022). Thus, the geometry studied in this experimental research is a simplified quasi-two-dimensional horizontal circular tank (figure 6).

Theoretical work deriving the eigenfrequenies of the horizontal circular tank was initially studied by Budiansky (1960). This solved anti-symmetric solutions of the eigenvalue problem in the transverse and longitudinal directions for a range of fill levels in a horizontal circular tank. This work was later extended to include symmetric solutions, limited to infinitely long cylinders (McIver 1989). A comprehensive review of the methodologies to solve the eigenvalue problem for the horizontal circular tank is given by Ibrahim (2005).

The present study is focused on a simplified horizontally orientated cylinder under vertical excitation, corresponding to the direction of gravity, g. Vertical accelerations on aircraft are common in turbulence and during taxiing. Furthermore, we focus on harmonic motion at the first limit of stability of the fluid, $f = 2f_n$, where f is the forcing frequency and f_n is the natural frequency of the nth mode. This condition is known to give rise to nonlinear free surface waves, known as Faraday waves, when the forcing amplitude exceeds a frequency-dependent critical value. This free surface deformation, also known as principal parametric resonance, results in sub-harmonic standing waves where the liquid column oscillates at half the forcing frequency. A comprehensive review of parametric sloshing research was completed by Ibrahim (2015). A range of experimental sloshing studies on cuboid geometries have previously investigated this phenomena (Jiang *et al.* 1996; Schultz *et al.* 1998; Bredmose *et al.* 2003; Bardazzi *et al.* 2024; Bardazzi *et al.* 2024).

To the best of the authors' knowledge Faraday waves have not been studied experimentally in a horizontal orientated cylinder. In fact, this geometry has received little attention experimentally. The first reported experimental study on this geometry investigated the free response of the fluid to validate liquid natural frequencies (MacCarty & Stephens 1960). Experimental work exciting the first anti-symmetric mode, under forced horizontal harmonic excitation, showed a soft-spring nonlinear response for $h/D = 0.30$ (Colville *et al.* 2023). Non-isothermal experiments investigating the sloshing induced pressure drop in a horizontal circular tank, under vertical excitation, have demonstrated pressure drops for various sloshing regimes using liquid water and water vapour (Saltari *et al.* 2024).

The isothermal experimental study carried out here extends that presented by Colville *et al.* (2024). Water is used as a surrogate for LH2 to enable cost effective experimentation and analysis of the fluid response, allowing key test cases to be identified under safe isothermal conditions. The objectives of this study are to develop an experimental methodology to quantify the wave kinematics of Faraday waves inside a simplified isothermal horizontal circular tank under vertical excitation. The experimental results will be compared with eigenfrequencies derived through linear potential flow. The sloshing tank will be subjected to harmonic vertical excitations in the frequency range of the first limit of fluid stability. The liquid kinematic motion will be characterised over a range of fill levels. This isothermal test campaign aims to improve our fundamental understanding of the mode shapes of this geometry and provide benchmark cases for future non-isothermal testing, which could improve our understanding of the characteristic pressure drop in non-isothermal cryogenic fuel tanks.

This paper is organised as follows. The fundamental liquid natural frequencies are derived for the horizontal circular tank in § 2. The experimental set-up, procedure and parameter space are described in § 3. Section 4 discusses the experimental results and compares the theoretical eigenfrequencies with experimental resonance values. Finally the work is concluded in § 5.

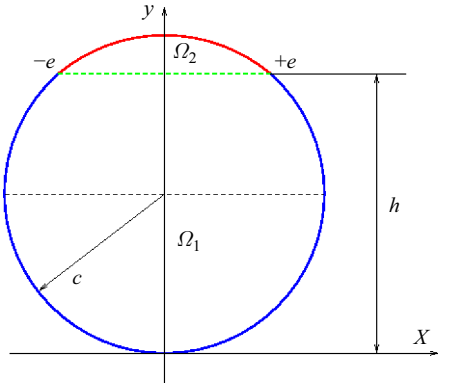

Figure 1. Configuration at rest of the two layer system in the cross-section of a horizontal circular tank.

2. Theoretical formulation

We consider a horizontal circular tank with diameter D and radius $c = D/2$, filled with two fluids which are immiscible, and denote by Ω_1 and Ω_2 the corresponding liquid and gas domains, as shown in figure 1 at rest. The density ratio $r = \rho_2/\rho_1$, of the lighter fluid (gas) to the heavier fluid (liquid), is arbitrary. The filling height is h measured from the bottom (south pole of the circular section). The half-length of the interface is denoted $e = \sqrt{c^2 - (h-c)^2}$. A conformal mapping (see McIver 1989) turns the inner circle $x^2 + (y-c)^2 \leqslant c^2$ into an infinite strip $\beta \in [-\pi : +\pi]$ and $\alpha \in]-\infty : +\infty[$; the mapping function that links the physical plane $z = x + iy$ to the transformed plane $\zeta = \alpha + i\beta$, reads

$$z = ih - e\tanh\left(\frac{\zeta}{2}\right), \quad \begin{cases} x = -\dfrac{e\sinh\alpha}{\cosh\alpha + \cos\beta}, \\ y = h - \dfrac{e\sin\beta}{\cosh\alpha + \cos\beta}. \end{cases} \tag{2.1}$$

The interface $(y = h, |x| < e)$ corresponds to $\beta = 0$. The Jacobian of the transformation is

$$J = \frac{\mathrm{d}z}{\mathrm{d}\zeta} = -\frac{e}{2}\left(1 - \tanh^2\left(\frac{\zeta}{2}\right)\right), \quad \text{with} \quad J_{interface} = -\frac{e}{1+\cosh\alpha}. \tag{2.2}$$

We introduce the angles $\beta_1 = (c-h)/c$ and $\beta_2 = (h-c)/c$ so that the line $\beta = \beta_i$ is the image of the circular arc (impermeable wall) bounding Ω_i for $i = 1$ or 2. The two angles β_i are opposite in sign and verify the identity $\beta_1 - \beta_2 = \pi$. Figure 2 illustrates the change of variables (2.1).

The kinematics of the two fluids are described in potential theory. The variables are the pressure p, the velocity potential ϕ and the free surface elevation η measured from the interface at rest. The corresponding boundary value problem (BVP) is formulated in the coordinate system (O, x, y) attached to the tank. This is a non-Galilean coordinate system. An impermeability condition is prescribed on the solid wall of the circular tank. Kinematic and dynamic nonlinear boundary conditions are prescribed along the interface between the two fluids. At the instantaneous interface of the two fluids, we impose the continuity of the pressure and the normal velocities

$$\phi_{1,t} + \frac{1}{2}(\vec{\nabla}\phi_1)^2 + G(t)y = r\left(\phi_{2,t} + \frac{1}{2}(\vec{\nabla}\phi_2)^2 + G(t)y\right), \quad \vec{\nabla}\phi_1 \cdot \vec{n} = \vec{\nabla}\phi_2 \cdot \vec{n}, \tag{2.3}$$

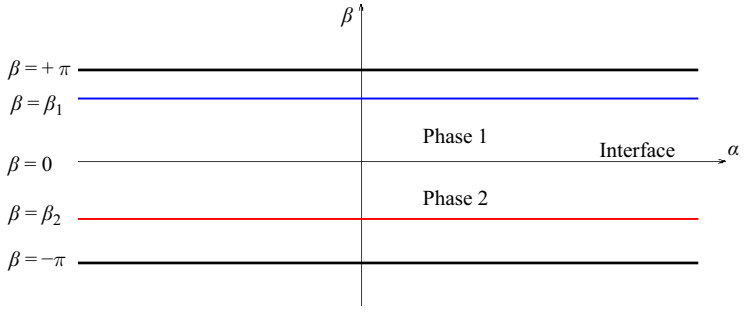

Figure 2. Transformed region that follows from the conformal mapping defined in (2.1). Images of the two fluid domains Ω_i and their boundaries.

where $\vec{n}$ is the normal vector along the interface, pointing to either side of this interface. Here, ϕ_1 and ϕ_2 describe the fluid motion in the (non-Galilean) coordinate system attached to the tank. On the solid wall of the tank, the velocity potentials ϕ_i verify a homogeneous Neumann boundary condition $(\phi_{i,\beta} = 0)_{i=1,2}$. The total vertical acceleration $G(t) = g - \omega^2\gamma\cos\omega t$ accounts for the acceleration of gravity g and the oscillating forced vertical acceleration of the tank, with forcing amplitude γ and angular frequency ω.

2.1. *Method of solution without forcing*

As a preliminary step we compute the eigenmodes and eigenfrequencies of the two-fluid dynamical system without forcing ($\gamma = 0$). This calculation follows from the linearisation of the BVP. The method of solution is exposed in McIver (1989) for a single phase. This is further developed for two phases in Scolan (2015). Calculation of eigenmodes and eigenfrequencies in a horizontal circular tank is also demonstrated by Faltinsen & Timokha (2012). The solution ϕ is sought as a harmonic function of time $\phi_i(x, y, t) = \Re(\varphi_i(x, y)e^{-i\omega t})$ with unknown circular frequency ω.

The linearised BVP for the two velocity potentials $(\varphi_i)_{i=1,2}$ is defined by

$$\begin{cases} \Delta\varphi_i = 0 & \text{in} \quad \omega_i,\ i = 1, 2, \\ \varphi_{i,\beta} = 0 & \text{on} \quad \beta = \beta_i,\ i = 1, 2, \\ \lambda\,(\varphi_1 - r\varphi_2) = (1 + \cosh\alpha)(r\varphi_{2,\beta} - \varphi_{1,\beta}) & \text{on} \quad \beta = 0, \\ \varphi_{1,\beta} = \varphi_{2,\beta} & \text{on} \quad \beta = 0, \end{cases} \tag{2.4}$$

where $\lambda = (e\omega^2)/g$. The general solutions which verify both Laplace equation and impermeability conditions on the wall read

$$\varphi_i(\alpha, \beta) = \int_0^\infty A_i(\tau)\cosh\tau(\beta - \beta_i)m(\tau\alpha)\mathrm{d}\tau, \quad i = 1, 2, \tag{2.5}$$

where the function m is either sine or cosine functions depending on the anti-symmetric or symmetric interface deformation, respectively. Rearranging algebraically and performing sine or cosine Fourier transform with respect to the variable α, we arrive at the integral equation for the unknown variables B and λ

$$(1 - r)B(\tau') = \lambda\int_0^\infty B(\tau)K(\tau, \tau')\mathrm{d}\tau, \quad \tau' \in [0, +\infty[, \tag{2.6}$$

with

$$f(\tau) = 1 - r\frac{\tanh\tau\beta_1}{\tanh\tau\beta_2}, \quad B(\tau) = A_1(\tau)\sqrt{\tau f(\tau)\sinh\tau\beta_1\cosh\tau\beta_1}, \tag{2.7}$$

and

$$K(\tau,\tau')=\sqrt{\frac{f(\tau)f(\tau')}{\tau\tau'\tanh\tau\beta_1\tanh\tau'\beta_1}}I(\tau,\tau'),\quad I(\tau,\tau')=\frac{2}{\pi}\int_0^\infty\frac{m(\tau\alpha)m(\tau'\alpha)}{1+\cosh\alpha}\mathrm{d}\alpha. \tag{2.8}$$

The function $I(\tau,\tau')$ is calculated analytically from Gradshteyn & Ryzhik (2014), see equation 3.982.1 on p. 510 therein.

It is clear that, when $r=0$ (vacuum above phase 1), the function f is unity and (2.6) reduces to equation (2.10) in McIver (1989). When the two fluids are identical, $r=1$, there is no possible motion of the interface inside the container and $\lambda\equiv 0$. When the filling ratio is half, i.e. $h=c=e$, then $\beta_1=-\beta_2=\pi/2$ and $A_1(\tau)=-A_2(\tau)$ whatever τ. By using the integral (2.6), we arrive at the result

$$\lambda(r)=\frac{1-r}{1+r}\lambda(0), \tag{2.9}$$

where $\lambda(0)$ is associated with the eigenfrequencies of the system fluidvacuum, i.e. with a real free surface. The factor $1-r/1+r$ is known as the Atwood number and the obtained result is consistent with those of Rayleigh (1882).

Integral (2.6) is interpreted as an eigenvalue problem; it is solved by using the Nyström technique (Nyström 1930). Numerically, we approximate the integral (2.6) with a Gauss–Laguerre quadrature formula

$$\int_0^\infty F(\tau)\mathrm{d}\tau\approx\sum_{j=1}^{N}F(\tau_j)w_je^{\tau_j}, \tag{2.10}$$

where τ_j are the N zeros of the Laguerre polynomials of order N and w_i are the corresponding weights. Those quantities are tabulated. By writing (2.6) at N points $\tau'=\tau_i$ and noting $B_i=B(\tau_i)$, we end up with the linear system

$$(1-r)B_i=\lambda\sum_{j=1}^{N}K(\tau_j,\tau_i)w_je^{\tau_j}B_j\quad\text{and}\quad\left(\boldsymbol{K}-\frac{1-r}{\lambda}\boldsymbol{I}_d\right)\boldsymbol{B}=0, \tag{2.11}$$

where $\boldsymbol{I}_d$ is the identity, $\boldsymbol{B}$ is the vector whose ith component is B_i and $\boldsymbol{K}$ is the matrix whose N eigenvalues $v_i=(1-r)/\lambda$ yield the N eigenfrequencies $\omega_i=\sqrt{((1-r)g)/ev_i}$ with $1\leqslant i\leqslant N$, of the linear dynamical system. As an alternative to the Gauss–Laguerre quadrature integration, the interval of integration in (2.6) can be turned into $[-1:1]$ by using the change of variable $u=2e^{-\tau}-1$. As a result a Gauss–Legendre quadrature integration is used.

2.2. *Method of solution with forcing*

If we consider now the vertical forced motion, the principle is quite similar. We expect to arrive finally at a standard Mathieu equation as described in Benjamin & Ursell (1954). The general solutions which verify both Laplace equation and impermeability conditions on the wall are the same as in (2.5), however, the functions A_i depend on time from now on. The continuity of the pressure and the normal velocity at the interface yields

$$(1-r)G(t)\eta(\alpha,t)=-\int_0^\infty f(\tau)A_{1,t}(\tau,t)\cosh(\tau\beta_1)m(\tau\alpha)\mathrm{d}\tau. \tag{2.12}$$

The kinematic free surface boundary condition at the interface gives

$$\eta_{,t}(\alpha, t) = -\frac{1}{e}(1+\cosh\alpha)\phi_{1,\beta}\Big|_{\beta=0} = \frac{1}{e}(1+\cosh\alpha)\int_0^\infty \tau A_1(\tau, t)\sinh\tau\beta_f m(\tau\alpha)\mathrm{d}\tau. \tag{2.13}$$

The new unknown function B is introduced as follows:

$$B_{,t}(\tau, t) = A_1(\tau, t)\sqrt{\tau f(\tau)\sinh\tau\beta_1\cosh\tau\beta_1}, \tag{2.14}$$

where the function f is given in (2.7). Substituting A_1 from (2.14) in (2.13) and performing a time integration, η is obtained

$$\eta(\alpha, t) = \frac{1}{e}(1+\cosh\alpha)\int_0^\infty B(\tau, t)\sqrt{\frac{\tau\tanh\tau\beta_1}{f(\tau)}}m(\tau\alpha)\mathrm{d}\tau, \tag{2.15}$$

where the constant of integration is discarded by invoking the mass conservation. Differentiating (2.14) in time, the function $A_{1,t}$ is introduced in the integrand of (2.12) yields

$$(1-r)G(t)\eta(\alpha, t) = -\int_0^\infty B_{,t^2}(\tau, t)\sqrt{\frac{f(\tau)}{\tau\tanh\tau\beta_1}}m(\tau\alpha)\mathrm{d}\tau. \tag{2.16}$$

Equating η obtained from (2.15) and (2.16), we arrive at

$$(1-r)G(t)(1+\cosh\alpha)\int_0^\infty B(\tau, t)\sqrt{\frac{\tau\tanh\tau\beta_1}{f(\tau)}}m(\tau\alpha)\mathrm{d}\tau = -e\int_0^\infty B_{,t^2}(\tau, t)\sqrt{\frac{f(\tau)}{\tau\tanh\tau\beta_1}}m(\tau\alpha)\mathrm{d}\tau. \tag{2.17}$$

The Fourier transform of this last (2.17) is performed with respect to the variable α

$$(1-r)G(t)B(\tau', t)\sqrt{\frac{\tau'\tanh\tau'\beta_1}{f(\tau)}} = -e\int_0^\infty B_{,t^2}(\tau, t)\sqrt{\frac{f(\tau)}{\tau\tanh\tau\beta_1}}I(\tau, \tau')\mathrm{d}\tau, \tag{2.18}$$

where I is given in (2.8). Using the function K introduced in (2.8), the integro-differential equation is finally obtained

$$(1-r)G(t)B(\tau', t) = -e\int_0^\infty B_{,t^2}(\tau, t)K(\tau, \tau')\mathrm{d}\tau. \tag{2.19}$$

If the function B is time harmonic with frequency ω and if $G = g$, the eigenvalue problem given in (2.6) is retrieved. The numerical discretisation of the integral in (2.19) is identical to the method exposed in the previous section. As a result a time differential system must be solved

$$e\boldsymbol{K}\boldsymbol{B}_{,t^2} + (1-r)G(t)\boldsymbol{B} = 0, \tag{2.20}$$

where $\boldsymbol{K}$ is the matrix whose elements are introduced in (2.11). The components of the vector $\boldsymbol{B}$ are the variable B calculated at the N zeros of the Laguerre polynomials of order N. We assume matrix $\boldsymbol{K}$ is diagonalisable and hence $\boldsymbol{K}$ can be written $\boldsymbol{K} = \boldsymbol{P}\boldsymbol{H}\boldsymbol{P}^{-1}$. The matrix $\boldsymbol{H}$ is diagonal and contains the N eigenvalues v_i of $\boldsymbol{K}$. The columns of the matrix $\boldsymbol{P}$ are the eigenvectors of $\boldsymbol{K}$. Those quantities follow from the calculation presented

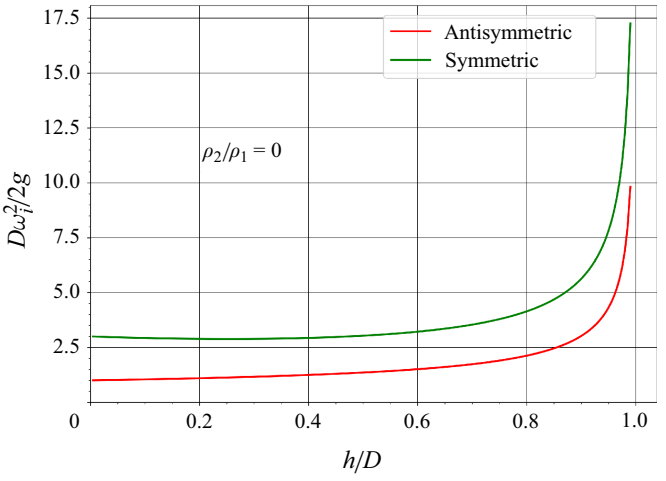

Figure 3. Non-dimensional eigenfrequency first mode for a varying fill level h/D.

in the previous section. As a consequence (2.20) is written for a vector $\boldsymbol{E} = \boldsymbol{P}^{-1}\boldsymbol{B}$, yielding the time differential system

$$eH\boldsymbol{E}_{,t^2} + (1-r)G(t)\boldsymbol{E} = 0. \tag{2.21}$$

Similar results are shown in Wright, Yon & Pozrikidis (2000) or in Kumar & Tuckerman (1994) but for another two-fluid system (infinite horizontal strips).

The ith line of (2.21) are standard Mathieu equations for the ith component E_i of the vector $\boldsymbol{E}$

$$E_{i,t^2} + \omega_i^2\left(1 + \frac{-\omega^2\gamma}{g}\cos\omega t\right)E_i = 0, \quad \omega_i = \sqrt{\frac{(1-r)g}{ev_i}}. \tag{2.22}$$

It is worth recalling that ω_i is the linear waves circular frequency without damping and forcing (see Rajchenbach & Clamond (2015)). This time differential (2.22) is abundantly discussed in the literature since the pioneering work by Benjamin & Ursell (1954). The standard Floquet stability analysis is performed in terms of the two parameters $p_i = 4\omega_i^2/\omega^2$ and $q_i = \omega^2\gamma p_i/2g$. The first limit of stability for symmetric free surface deformation occurs when $p_2 = 1$. The two-fluid solution has been solved analytically using conformal mapping, which provides an almost analytical formulation for both the computation of linear eigenfrequencies and the derivation of the Mathieu equation. It should be noted that, for the case where, $\rho_2/\rho_1 = 0$, the classical multimodal approach presented in Faltinsen & Timokha (2009) yields equivalent results.

The resulting non-dimensional eigenfrequencies of the first symmetric and anti-symmetric modes are expressed for all fill levels h/D with a constant density ratio $\rho_2/\rho_1 = 0$ shown in figure 3.

Figure 4 shows the potential range of density ratios in a sub-cooled LH2 fuel tank. The liquid phase density, ρ_{LH2}, is $72.3\,\mathrm{kg\,m^{-3}}$ assuming the constant temperature $T = 20\,\mathrm{K}$. The gas density is displayed between the triple and critical temperatures of hydrogen, $T_t = 13.97\,\mathrm{K}$, and $T_c = 33.15\,\mathrm{K}$, over the pressure range 1–10 bar. The largest density ratio, $\rho_{H2}/\rho_{LH2} = 0.19$, occurs at the highest pressure considered and the lowest gas temperature for this pressure. The smallest density ratio, $\rho_{H2}/\rho_{LH2} = 0.01$, occurs at the smallest pressure considered and the highest temperature (below the critical

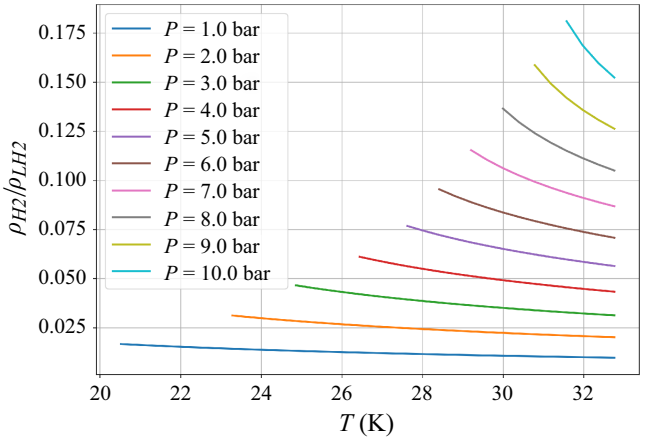

Figure 4. Density ratio range in a sub cooled LH2 fuel tank (Bell *et al.* 2014). Liquid hydrogen density, ρ_{LH2}, is 73.2 kg m^{-3} assuming the constant temperature $T = 20$ K. The gas density, ρ_{H2}, is considered in the pressure range of $P = 1{-}10$ bar at temperatures between the hydrogen triple and critical temperatures $T_t = 13.97$ K and $T_c = 33.15$ K, respectively.

temperature T_c) at this pressure. This indicates that the density ratio in an LH2 fuel tank varies significantly depending on the operating pressure. It is important to quantify the effect this change in density ratio could have on the eigenfrequencies of the tank.

The non-dimensional eigenfrequencies $D\omega_2^2/2g$ of the first symmetric mode in terms of the density ratio are expressed in figure 5. These are expressed for three fill levels $h/D =$ 0.3, 0.5 and 0.67. The density ratio range considered for a LH2 fuel tank is displayed through the yellow region on figure 5. This shows a significant decrease in the eigenvalue $D\omega_2^2/2g$ where the density ratio is large.

At small density ratio only a small change in the eigenfrequency exists from the reference case $\rho_2/\rho_1 = 0$. In the subsequent airwater sloshing experiment, the first symmetric mode eigenfrequency is obtained from figure 5, corresponding to a density ratio of $\rho_{air}/\rho_{water} = 0.0012$, as shown in the inset of figure 5. The corresponding eigenfrequencies of the first symmetric mode for each fill level are expressed in table 1.

3. Experimental techniques

3.1. *Experimental set-up*

The experimental apparatus and coordinate system is displayed in figure 6, where (0, 0) are coordinates of the tank centre. The sloshing tank is identical to that described by Colville *et al.* (2023), a brief description is given here for completeness. A narrow cast acrylic sloshing tank with transparent faces is manufactured, with a rubber infused cork gasket clamped between each face and the geometry. This is secured with a series of bolts ensuring a watertight seal. The sloshing tank has depth $d = 40 \pm 0.02$ mm and diameter $D = 400 \pm 0.02$ mm (as displayed in figure 6). The small depth relative to the diameter aims to suppress longitudinal modes, resulting in quasi-two-dimensional fluid motion in the tank.

Figure 7 shows the experimental set-up. The main components in the experimental set-up are, the rigid frame, electromechanical actuator, manufactured sloshing tank, bearings and rails. The frame is vertically mounted and secured to the ground and laboratory roof. The electromechanical actuator is fixed to the frame and the sloshing tank is directly fitted to the actuator rod. Four vertically orientated self-lubricating bearings are attached to the

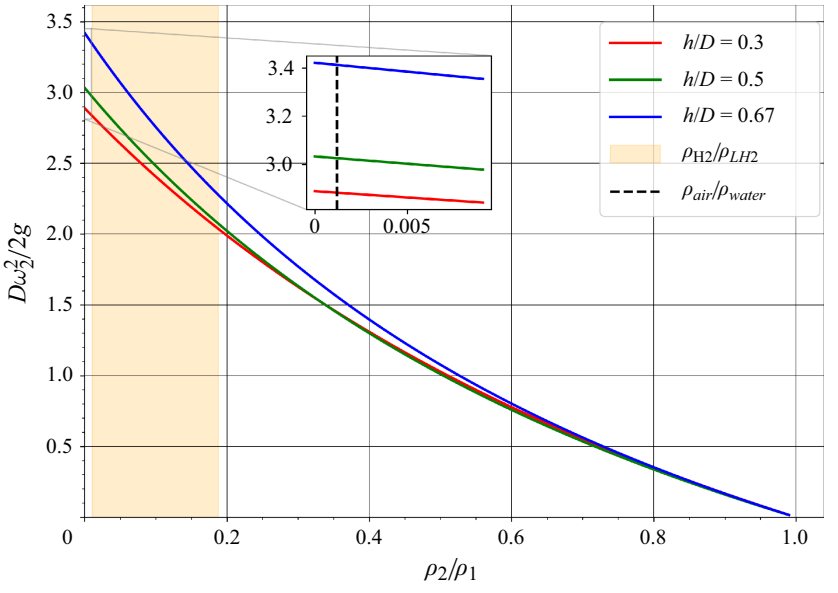

Figure 5. Variation of first symmetric mode in terms of density ratio. The density ratio of air–water ρ_{air}/ρ_{water} and the maximum and minimum values of the density ratio range considered in figure 4 are highlighted.

h/D	f_2 (Hz)	f/f^*	γ/D
0.3	1.893	$0.923 \leqslant f/f^* \leqslant 1.082$	$0.005 \leqslant \gamma/D \leqslant 0.01$
0.5	1.938	$0.973 \leqslant f/f^* \leqslant 1.032$	$0.005 \leqslant \gamma/D \leqslant 0.01$
0.67	2.060	$0.930 \leqslant f/f^* \leqslant 1.026$	$\gamma/D = 0.005$

Table 1. Parameter space: $h =$ fluid fill level, $D =$ tank diameter, $f_2 =$ first symmetric linear wave frequency, $f =$ forcing frequency, $f^* = 2f_2$ and $\gamma =$ forcing amplitude.

tank. Two parallel rails are inserted through the bearing pairs and connected to the rigid frame at their end points. The rails ensure the tank motion is in a single vertical degree of freedom and the self lubricating bearings minimise the friction in the mechanical system.

Data are acquired through a Photron Fastcam Sa4 high-speed camera (HSC) with a 70–300 mm lens. The HSC captures images of the sloshing motion within the partially filled container under excitation. The images have a spatial resolution 1024 × 1024 pixels and are acquired at 60 frames per second with a shutter speed range of 1/12 000–1/15 000s. The free surface displacement is quantified through images post-processed using an image processing algorithm, this is described in greater detail in § 3.2. Two high-intensity lights are positioned at either edge of the geometry, their light is reflected and diffused off a white background screen directly behind the geometry. This creates homogeneous lighting conditions minimising reflections and glare on the tank. A similar lighting set-up has been employed previously in sloshing experiments (Gambioli *et al.* 2019; Colville *et al.* 2023). The high intensity lights create a bright field of view behind the sloshing tank. This allows for high camera shutter speeds, ensuring sharp images are captured where the tank and fluid are moving at a relatively high velocity.

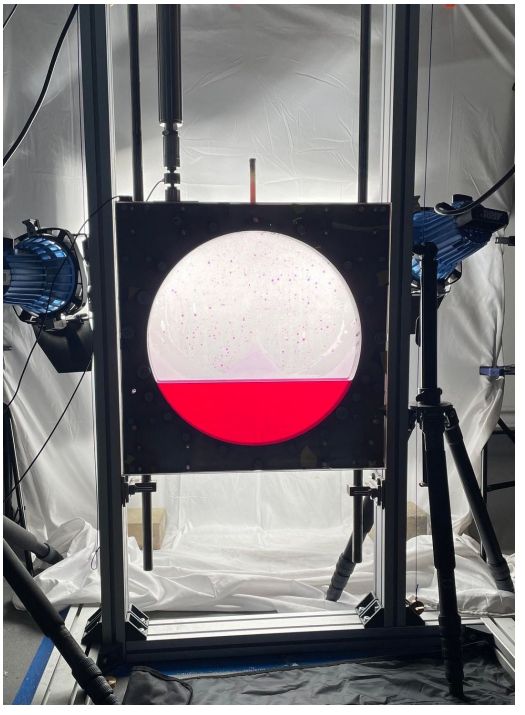

Figure 6. Experimental set-up.

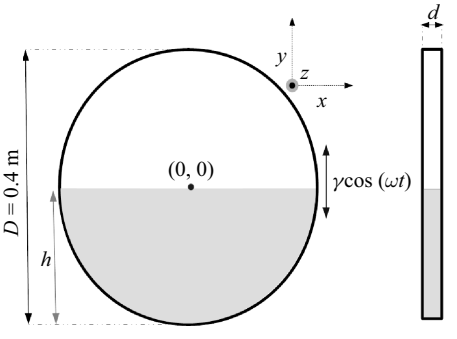

Figure 7. Sketch of tank coordinate system, where (0, 0) are the tank centre coordinates.

3.2. *Image processing*

An image processing algorithm (IPA) extracts the free surface profile for the images acquired through the HSC. The HSC remains in a fixed field of view and the sloshing tank is a moving region of interest (ROI) within this fixed field of view. Therefore, the first step of the IPA is to identify the ROI (circular sloshing tank) for each individual frame.

The equation of a circle is given by $(x-a)^2+(y-b)^2=c^2$ where (a, b) are the circle centre coordinates and c is the radius of the circle. The hough gradient method (Duda & Hart 1972) is used to identify these three parameters using gradient-based edge detection from the input greyscale image.

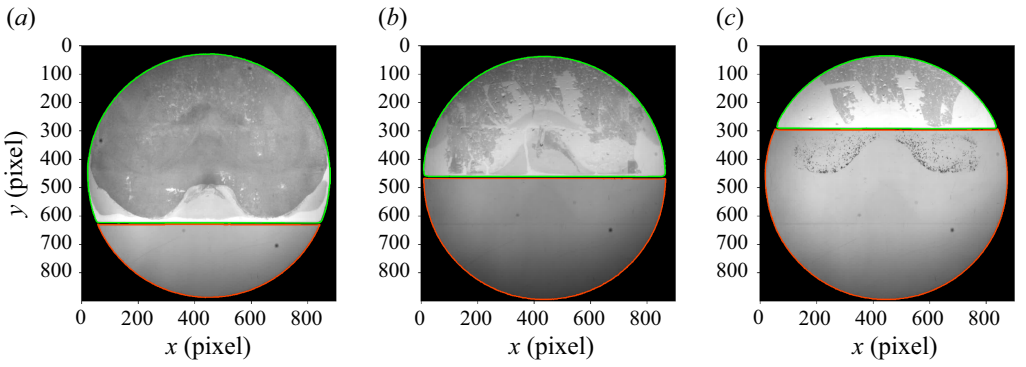

Figure 8. Static fluid reference cases with extracted liquid (orange) and gas (green) phase overlaid, respectively. (*a*) $h/D = 0.3$; (*b*) $h/D = 0.5$; (*c*) $h/D = 0.67$.

Once the ROI has been identified the ROI is converted from a greyscale image to a binary image using a fixed level threshold. The contours of the binary image are then extracted for the gas and liquid phases respectively. If the contour curves fail to extract these two phases then the initial threshold operation has failed to extract a continuous line along the free surface. This may occur due to spurious lighting in the image breaking the free surface at certain fluid/tank displacements. In this case morphological operations are applied to the image. Initially the 'erosion' operation is applied, this removes pixels from the binary image. Once the pixels connecting the liquid and gas phases are removed the respective phases are independent of each other. Finally, the 'dilation' operation is applied to both structures (liquid and gas) to retain the dilated pixels. This simple effective algorithm which combines a constant threshold and morphological operations requires little computational effort to process a large number of images (Maragos & Schafer 1990). Figure 8 shows the extracted coordinates of the liquid and gas phases for static fluid cases.

The image is converted from pixel coordinates to world coordinates using the known diameter of the tank. Subsequently the kinematics of the free surface anti-nodes (for a symmetric mode) i.e. the left and right sidewalls (LS and RS) and the free surface centre (FSC) are characterised.

Thus, the amplitude of the liquid displacement for each respective anti-node (LS, RS and FSC) through a sloshing cycle is analysed hereafter. This amplitude is defined as half of the peak to trough wave height of the sloshing liquid see figure 10(*b*). We term this the sloshing wave amplitude, A_s.

3.3. *Experimental parameter space*

The *parameter* space in this work focuses on symmetric modes excited in the region of sub-harmonic resonance. The experimental campaign failed to excite stable anti-symmetric modes in this frequency region. The viscous stress in the static fluid was too large to maintain a stable mode. Thus, when the forcing amplitude overcame the viscous stress the wave amplitude grew rapidly. This resulted in highly nonlinear breaking waves. In some cases a portion of fluid wrapped around the circumference of the tank before breaking into the bulk fluid on the opposing sidewall. In future work a method to initially disturb the fluid could be implemented (Bredmose *et al.* 2003). This would likely allow smaller forcing amplitudes to be tested, which may generate stable anti-symmetric mode shapes.

A harmonic vertical excitation $y(t) = \gamma \cos(\omega t)$ is applied to the partially filled container, where $\omega = 2\pi f$. Therefore, in this experiment there are three variable

h/D	Pixel size (mm)	h_{actual} (mm)	$h_{measured}$ (mm)	a_{liquid} (m^2)	$a_{measured}$ (m^2)
0.30	0.468	120	119.23 ± 0.468	0.0317	0.0329
0.50	0.475	200	200.27 ± 0.475	0.0628	0.0630
0.67	0.473	268	268.52 ± 0.473	0.0895	0.090

Table 2. Static case uncertainty quantification.

parameters: the forcing frequency f, the forcing amplitude γ and the fluid fill level h. Table 1 presents the range at which these parameters are tested in non-dimensional form, and the first symmetric linear wave frequency f_2 for the corresponding fill levels tested. The forcing frequency f is in the region of principal parametric resonance, $2f_2$, of the fundamental symmetric mode, $n = 2$, where one wavelength is equal to the length of the static free surface. Hereafter, we denote $2f_2$ as f^*. The mode is symmetric through the tank centreline $x = 0$. Two nodal lines (stationary points) are present half-way between the tank sidewall and the tank centre, and three anti-nodes are present at the tank sidewalls and the tank centreline.

Two fundamental comparisons in the steady-state liquid motion regime are analysed in this parametric study. The sloshing response for a fixed fill level, $h/D = 0.3$, and three different forcing amplitudes, $\gamma = 2$ mm, 3 mm and 4 mm, and the sloshing response for three different fill levels, $h/D = (0.3, 0.5, 0.67)$, with a fixed forcing amplitude $\gamma = 2$ mm.

3.4. *Experimental procedure*

Assuming a constant density of water at room temperature, the necessary mass of water required to fill the tank to the desired fill level is calculated. A red liquid dye is added to the water before the mass measurement to increase contrast between the water and air thus improving image post processing (see § 3.2). This is measured using scales to a precision of ± 0.005 kg. The tank is then filled with water to a desired fill level.

Initially transient tests are completed, this determines the number of cycles needed for transient effects to dissipate, thus informing where the liquid has reached a steady-state response. Following this determination the actuator operates for a prescribed 350 cycles until the steady-state regime is reached. Once this point is reached and the HSC shutter is activated and images are recorded for 30 s. After this period the actuator stops and the liquid motion decays to a quiescent state. This procedure is completed for all steady-state test cases, where the fluid is initially at rest.

3.5. *Experimental uncertainties*

First, uncertainties are quantified where there is no liquid motion; figure 8(*a–c*) shows the static reference cases for the three fill levels tested. The pixel resolution of these three cases is calculated through the known diameter of the tank. Table 2 presents the image resolution for each fill level tested, the actual fluid height, h, of the desired fill level, the corresponding free surface elevation calculated from each static image through the IPA, $h_{measured}$, the actual area of the static liquid, a_{liquid}, and the measured area form the IPA, $a_{measured}$.

The percentage uncertainties, $\delta a\%$, between the measured and actual values in the static area are expressed in table 3. The absolute uncertainty, u_{abs}, in the fluid height is also displayed in table 3. This is expressed through the error between $h_{measured}$ and h_{actual} combined with the pixel resolution uncertainty for each respective fill level.

h/D	δa (%)	u_{abs} (mm)
0.30	3.79	±0.901 mm
0.50	0.32	±0.546 mm
0.67	0.56	±0.703 mm

Table 3. Percentage uncertainty in fluid area, δa, and absolute uncertainty, u_{abs}, in fill level height.

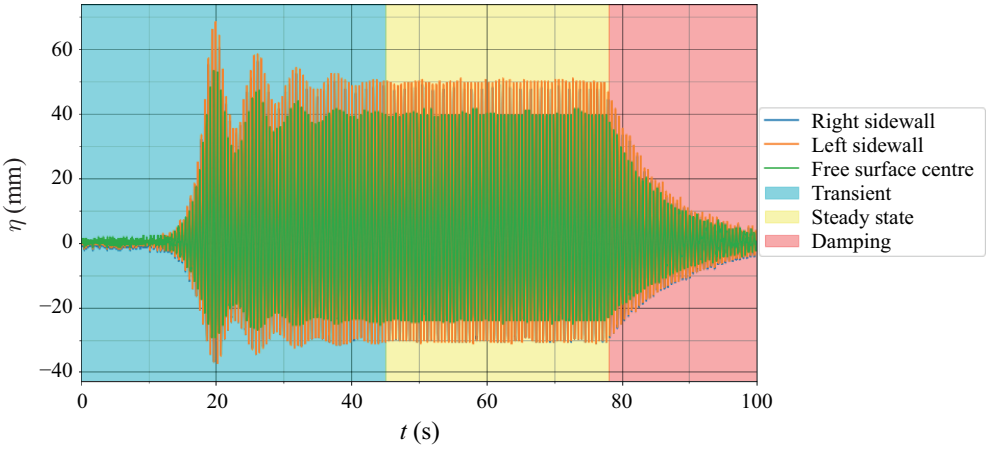

Figure 9. Free surface elevation (η) against time (t) showing transient, steady-state and damping regimes for the fundamental symmetric mode anti-nodes; 0.3 fill level, $\gamma = 4$ mm and $f = 3.86$ Hz.

3.6. *Repeatability tests*

A total of 123 test cases were performed and measured, shown in figures 11 and 15. Due to time constraints, repeatability tests (consisting of three case repetitions) are only completed for 16 selected test cases. The standard deviation of these repeat tests is multiplied by three to cover 99 % of the possible data points. This is presented through error bars in figures 11 and 15. Generally, the largest standard deviation in the repeat tests occurs where the sloshing wave amplitude, A_s, is largest. The smallest standard deviation occurs where there is little fluid motion.

4. Results and discussion

4.1. *Symmetric modes and fluid regimes*

In the majority of symmetric mode test cases, accelerations are small enough to prevent wave breaking at the interface. Figure 9 shows three general regimes exhibited by a liquid in a partially filled container under excitation. The fluid is initially at rest and a harmonic excitation, $y(t) = \gamma \cos(\omega t)$, is applied to the tank. Initially, figure 9 (blue) shows a transient phase exhibiting 'beating' phenomena. After a finite time the beating signal dissipates and the fluid reaches a steady-state regime, figure 9 (yellow). In the steady-state regime, where the sloshing wave amplitude, A_s, is relatively small, the signal is periodic over one cycle and the wave height remains constant. Once the tank excitation is halted there is a damping period, figure 9 (red). The liquid continues to oscillate and the sloshing wave amplitude, A_s, decays with respect to time, eventually the free surface

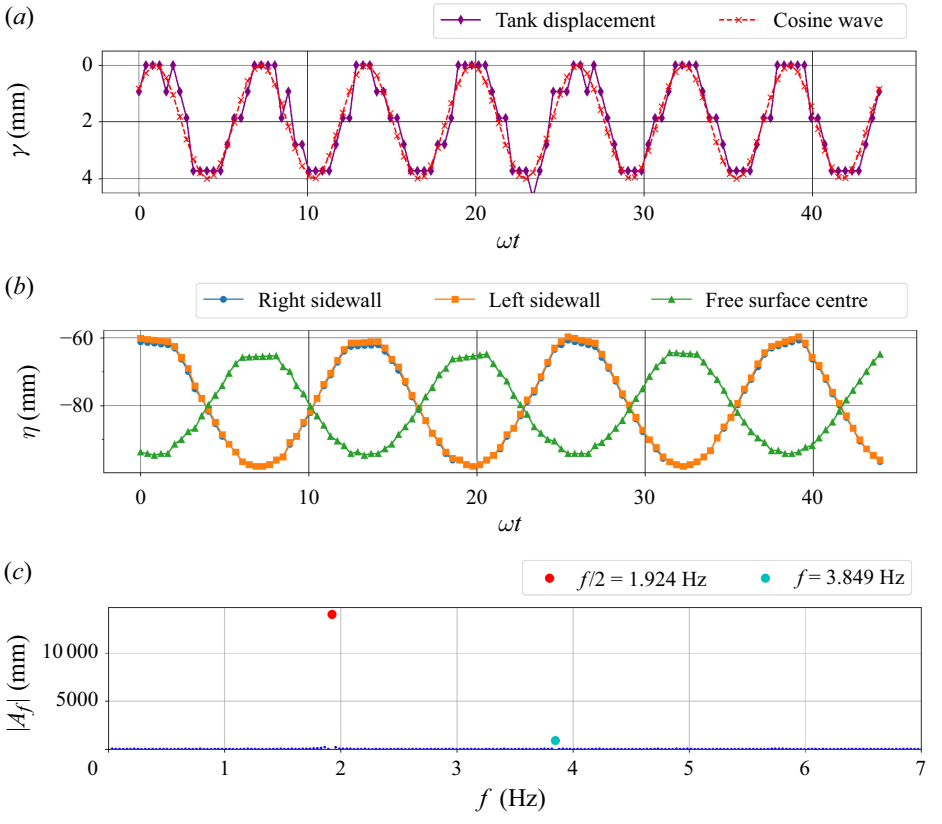

Figure 10. The 0.3 fill level, forcing frequency $f = 3.850$ Hz ($f/f^* = 1.016$) and forcing amplitude $\gamma = 2$ mm: (*a*) tank displacement; (*b*) steady-state sloshing wave amplitude of the (FSC, RS and LS); (*c*) DFT of sloshing wave amplitude at the FSC.

returns to quiescent conditions. This discussion is devoted to the steady-state nonlinear fluid response, figure 9 (yellow).

4.2. *Steadystate regime*

Figure 10(*a*) shows the tank displacement where the forcing amplitude is $\gamma = 2$ mm and the forcing frequency is $f = 3.850$ Hz ($f/f^* = 1.016$). The corresponding fluid displacement of the extracted points of interest on the free surface is displayed in figure 10(*b*). The RS and LS show symmetry and the FSC is out of phase with the respective sidewalls. In general, the maximum tank displacement occurs at the same time as the maximum fluid displacement (sidewall or FSC).

Performing a discrete Fourier transform (DFT) on the steady-state time series we can analyse the harmonic Fourier amplitudes, A_f, in the frequency domain. Applying a DFT to the time series data gives a frequency resolution of ± 0.033 Hz. Figure 10(*c*) shows the result from the FSC displacement, where two peaks at 1.924 Hz and 3.849 Hz are shown. The first peak shows sub-harmonic resonance where the dominant amplitude of the signal occurs at approximately half of the forcing frequency. This is confirmation of Faraday waves generated at the fundamental symmetric mode. The second peak shows a harmonic near the forcing frequency. The presence of this mode indicates temporal

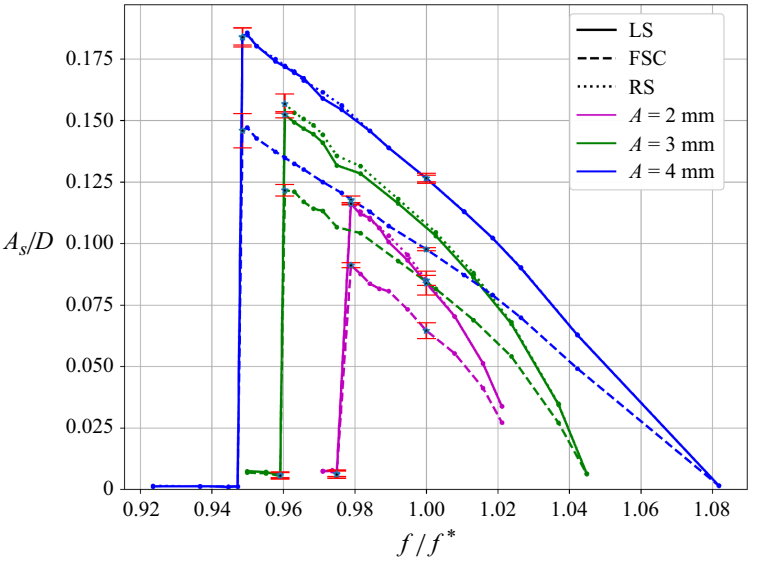

Figure 11. Steady-state sloshing wave amplitude, A_s (FSC, RS and LS) expressed against excitation frequency for different forcing amplitudes and a constant fill level $h/D = 0.3$.

asymmetry which can be described through the interaction of the fundamental mode and its second harmonic (Jiang *et al.* 1996). This harmonic was common for all test cases owing to the asymmetric (non-monochromatic) nature of Faraday waves. Such temporal asymmetry and harmonic interactions are linked to wave breaking, thus characteristics of near breaking standing waves for different fill levels will be discussed in more detail in § 4.4.

4.3. *Amplitude response to varying driving terms and fluid fill levels*

Sloshing wave amplitudes, A_s, are expressed in figure 11. As mentioned previously this is defined as half of the anti-node wave height (figure 10*b*). This amplitude is made dimensionless through the diameter, D, of the sloshing tank. The standard deviation of repeated test cases is displayed through error bars on figure 11.

Firstly, the sloshing wave amplitude dependence on the forcing frequency is investigated with a constant fill level, $h/D = 0.3$. Three forcing amplitudes, $\gamma = (2,3,4)$ mm, are tested. The forcing frequency, f, is made dimensionless with twice the frequency of the first symmetric mode, f^*, for $h/D = 0.3$. Figure 11 shows an amplitude 'jump' from near zero to the maximum sloshing amplitude. We term the maximum sloshing amplitude for each γ the experimental resonance frequency. An amplitude 'jump' is characteristic of nonlinear resonance (Jiang *et al.* 1996) and is displayed for all forcing amplitudes tested. As the forcing amplitude is increased the sloshing wave amplitude increases. The frequency ratio f/f^* at which experimental resonance occurs decreases with increasing γ. Experimental resonance occurs at $f/f^* = 0.980$ for $\gamma = 2$ mm, $f/f^* = 0.960$ for $\gamma = 3$ mm and $f/f^* = 0.949$ for $\gamma = 4$ mm. The nonlinearity increases with higher forcing amplitudes and subsequent sloshing wave amplitudes i.e. f/f^* decreases from linear potential flow theory where f/f^*=1. The frequency ratio is below one for all forcing amplitudes showing a soft-spring nonlinear response. As defined for flat bottom geometries, a soft-spring response is characteristic of deep water conditions above the critical fluid depth (Ibrahim 2005). We show soft-spring behaviour is observable in this geometry. We expect that lower fill levels

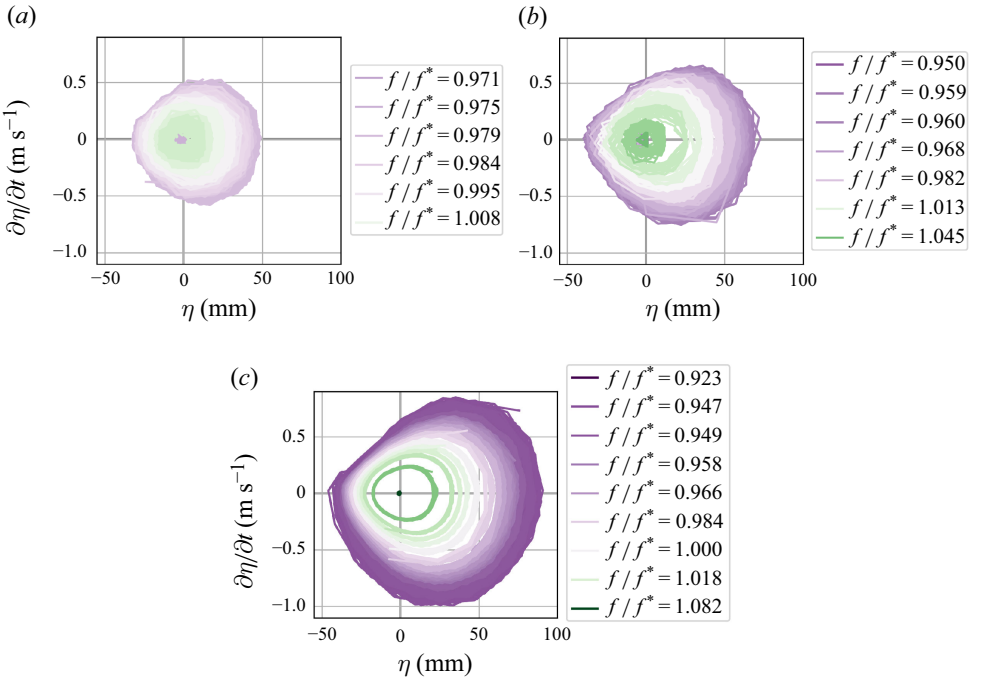

Figure 12. Velocity phase plane diagrams (0.3 fill level) where η is the FSC elevation, f is the forcing frequency and f_2 is the first symmetric linear wave frequency: (*a*) forcing amplitude $\gamma = 2$ mm; (*b*) forcing amplitude $\gamma = 3$ mm; (*c*) forcing amplitude $\gamma = 4$ mm.

will produce hard-spring behaviour (shallow water conditions). To the best of the authors' knowledge a critical fluid depth has not been determined for this geometry.

Additionally, figure 11 shows the sloshing wave amplitude, A_s, of the three anti-nodes present in the symmetric mode for all three tested forcing amplitudes. This shows the largest sloshing amplitude, for all forcing amplitudes, occurs at the LS and RS with the FSC anti-node consistently showing smaller displacements. This is true for all test cases displayed in figure 11.

4.3.1. *Wave steepness*

The nonlinearity in the liquid response can also be visualised through phase plane plots for each test case. The velocity, $\partial\eta/\partial t$, and displacement, η, of the FSC anti-node for the three tested forcing amplitudes of the $h/D = 0.3$ fill level are displayed in figure 12. As the forcing amplitude increases figure 12 displays a qualitative change in the shape of the phase plane diagram. Unsurprisingly even the smallest forcing amplitude case $\gamma = 2$ mm, figure 12(*a*), differs from a linear circular orbit. Figure 12(*c*) shows the highest forcing amplitude $\gamma = 4$ mm. The bounded orbits characterising the liquid kinematic response display asymmetries between the peak and trough values. Notably, the increased displacement of the wave crest (elevation above the static free surface) is displayed for higher forcing amplitudes. The wave crest amplitude is shown to increase more significantly compared with the wave trough amplitude.

This can also be displayed by comparing the mode shapes of figure 13(*a–c*). Figure 13 shows a constant fill level of $h/D = 0.3$ with the three tested forcing amplitudes. The free surface profile at the maximum and minimum amplitude of the FSC is displayed for every test case. We observe the sloshing wave amplitude, and subsequently the wave steepness, is

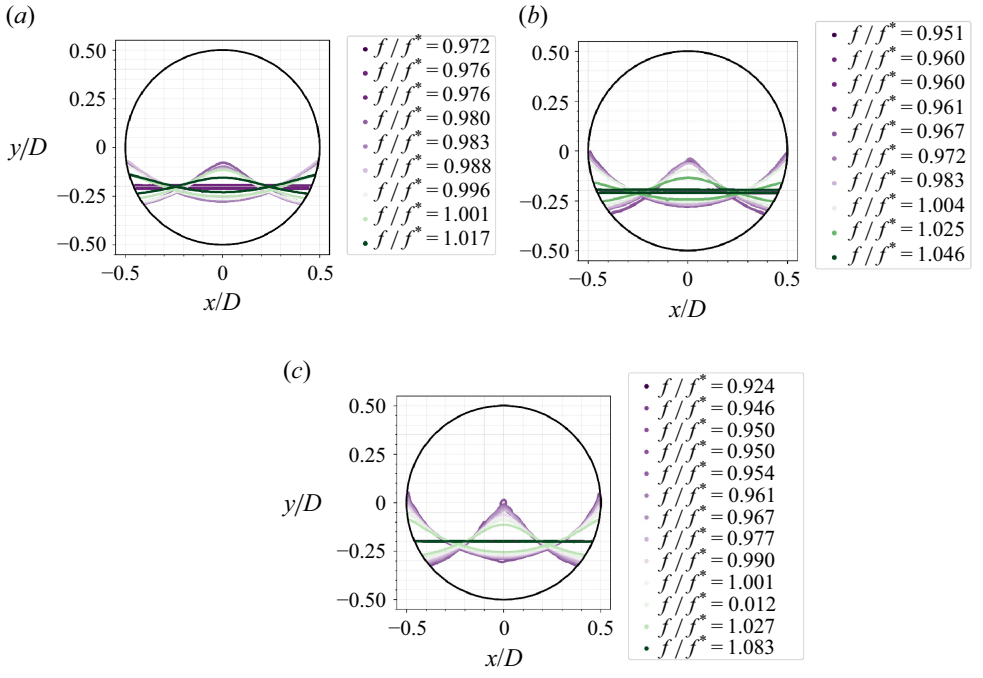

Figure 13. The 0.3 fill level maximum and minimum free surface centre elevation, for all tested frequencies: (*a*) forcing amplitude, $\gamma = 2$ mm; (*b*) forcing amplitude, $\gamma = 3$ mm; (*c*) forcing amplitude, $\gamma = 4$ mm.

increased as the forcing amplitude is increased. Here, the forcing amplitude is small ($\gamma =$ 2 mm) and the difference in wave crest and wave trough height from the static free surface is small. As the forcing amplitude is increased the wave height above the static free surface steepens. This is not replicated in the wave trough, which remains broad. This results in a smaller trough displacement at the tank centreline. Thus, for higher forcing amplitudes and higher sloshing wave amplitudes we observe increased asymmetry between the wave crest and trough. This nonlinearity was also reported through a fully nonlinear finite difference model of a sloshing liquid in a rectangular tank (Frandsen 2004).

The spatial profiles of the free surface across a temporal wave cycle are displayed in figure 14 for the resonant sloshing wave amplitude where $\gamma = 4$ mm. Figure 14(*a*) shows the increasing wave elevation and figure 14(*b*) shows the decreasing wave elevation. The sloshing wave amplitude (FSC) for this case is, $A_s = 58$ mm ($f/f^* = 0.949$). We define the wavelength (static free surface) as L where $L = 2c$. The wave steepness can be calculated by, $2A_s/L$, where, $2A_s$, is the total wave height and, L, is the wavelength, where, $h/D = 0.3$, the wavelength is, $L = 0.367$ m. This gives a wave steepness of 0.32. This case shows no evidence of wave breaking or air entrainment. It should be noted that the wavelength, L, is taken from the static water condition. However, due to the curved boundary of the geometry the physical length of the wave between the left and right sidewall changes as the liquid oscillates.

The overall mode shapes as the elevation increases and decreases in figure 14(*a*,*b*) show significant asymmetries. The free surface has near vertical sides either edge of the crest peak as the wave elevation descends, see figure 14(*b*). This case shows clear temporal asymmetry corresponding to different mode shapes (at a constant time interval) as the wave ascends and descends. This has been discussed previously for steep Faraday waves (Jiang *et al.* 1996; Bredmose *et al.* 2003). Similarities in steep sides as the wave descends

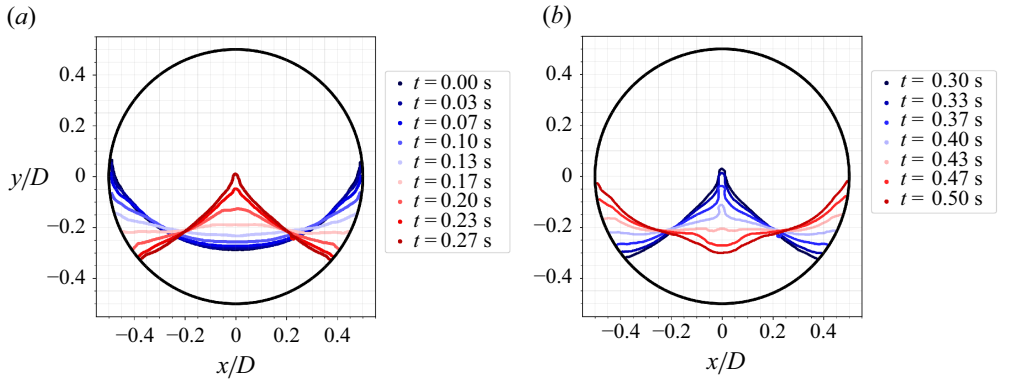

Figure 14. Wave profile 0.3 fill level, $\gamma = 4$ mm, $f = 3.595$ Hz: (*a*) increasing wave elevation through free surface centre; (*b*) decreasing wave elevation through the FSC.

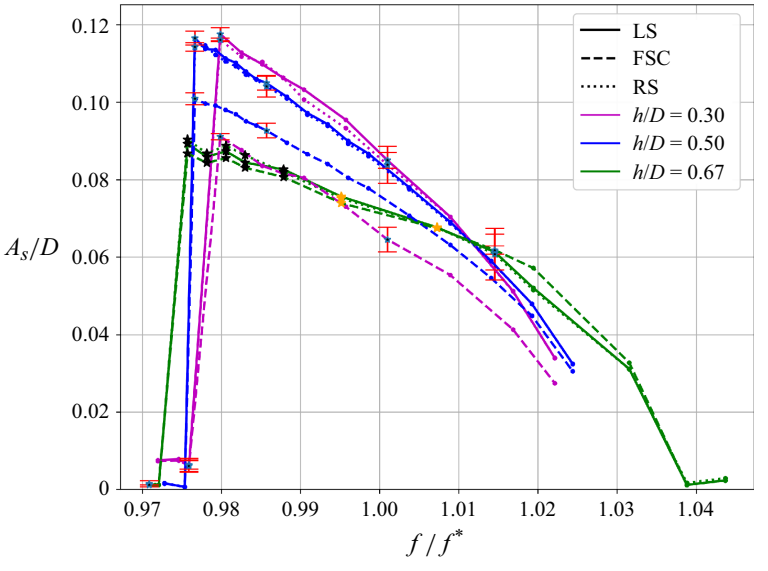

Figure 15. Steady-state sloshing wave amplitude (FSC, RS and LS) expressed against excitation frequency for three different fill levels, $h/D = (0.3, 0.5, 0.67)$. Black markers indicate wave breaking, orange markers indicate period tripling, all other markers are non-monochromatic waves.

are clear between this case and Bredmose *et al.* (2003). However, as the elevation descends the crest shape is narrower. The double crested peak reported by Jiang *et al.* (1996); Bredmose *et al.* (2003) is not observed for this fill level.

Figure 15 shows the sloshing wave amplitude for three fill levels, $h/D = (0.3, 0.5, 0.67)$, and a constant forcing amplitude, $\gamma = 2$ mm. Once again amplitude jumps are observed for all cases. The amplitude jumps occur at frequency ratios: $f/f^* = 0.980$ for $h/D = 0.30$, $f/f^* = 0.977$ for $h/D = 0.50$ and $f/f^* = 0.976$ for $h/D = 0.67$. Accordingly, the largest fill level tested shows the greatest nonlinearity and the smallest sloshing wave amplitude at experimental resonance. The lowest fill level tested shows the highest sloshing amplitude at experimental resonance and the closest experimental resonant frequency to linear potential flow theory. The fill level, $h/D = 0.67$, has a significantly smaller resonant sloshing wave

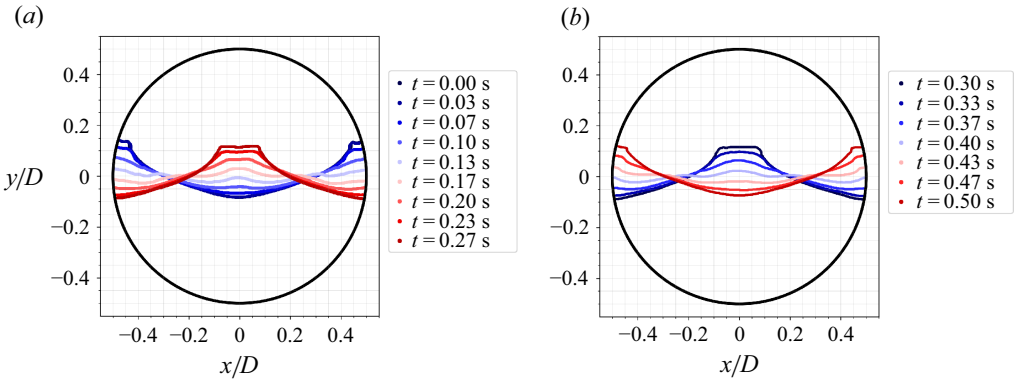

Figure 16. Wave profile 0.5 fill level, $\gamma = 2$ mm, $f = 3.785$ Hz: (*a*) increasing wave elevation through the FSC; (*b*) decreasing wave elevation through the FSC.

amplitude, where $h/D = 0.3$ and 0.5 there is little difference in the sidewall sloshing wave amplitude. The difference in the sloshing wave amplitude between the sidewalls and the FSC has already been highlighted for the 0.3 fill level. Figure 15 shows that the difference in magnitude between the sidewalls and the FSC decreases for higher fill levels. The magnitude of the anti-nodes where the $h/D = 0.67$ is almost symmetric. The decreased magnitude difference between the anti-nodes (and the overall decreased sloshing wave height) for the highest fill levels may be attributed to the geometry boundaries. At higher fill levels (above $h/D = 0.5$) the geometry boundary curves toward the tank centreline. Therefore, as the liquid is excited the wall 'run up' may be suppressed by this geometric constraint. This may explain the decreased wave elevation at the sidewalls and the overall decreased sloshing wave amplitude. Small fluctuations are visible in figure 15 for the 0.67 fill level, black markers. At these amplitudes wave breaking at the sidewalls was present. As the fluid elevation increased at the sidewall it collapsed from the inclined circumference causing spray and some air entrainment. It is expected that this energy dissipation has caused these fluctuations. The wave breaking threshold is reached at a significantly smaller sloshing amplitude where the fill level is 0.67, once again we believe this is significantly effected by the tank geometry. In figure 15 sloshing wave amplitudes with orange markers signify period tripling cases which will be discussed in § 4.4.

Similarities in the crest shape are observed between the 0.5 and 0.67 cases showing 'double peaked' and 'table top' crests similar to that described by Jiang *et al.* (1996); Bredmose *et al.* (2003). A case displaying a 'table top' crest is displayed in figure 16. Overall, comparisons of the free surface profile with the rectangular tank are 'delicate', even though some features described are similar.

4.4. *Frequency domain analysis and period tripling*

Generally, as discussed previously, for all test cases the dominant frequency occurs at half of the forcing frequency, $f/2$, figure 10(*c*). A comparably smaller magnitude harmonic also occurs at the forcing frequency, f. As previously stated the interaction between the dominant fundamental mode and the second temporal harmonic lead to temporal asymmetry in the Faraday waves. However, in the frequency domain of the case displayed in figure 14, additional harmonics are present. This is displayed through the DFT and phase plane plots in figure 17(*a*,*b*). A range of sub- and super-harmonics at intervals of 0.6 ± 0.033 Hz are present. This is $f/6$ harmonic intervals from the forcing frequency.

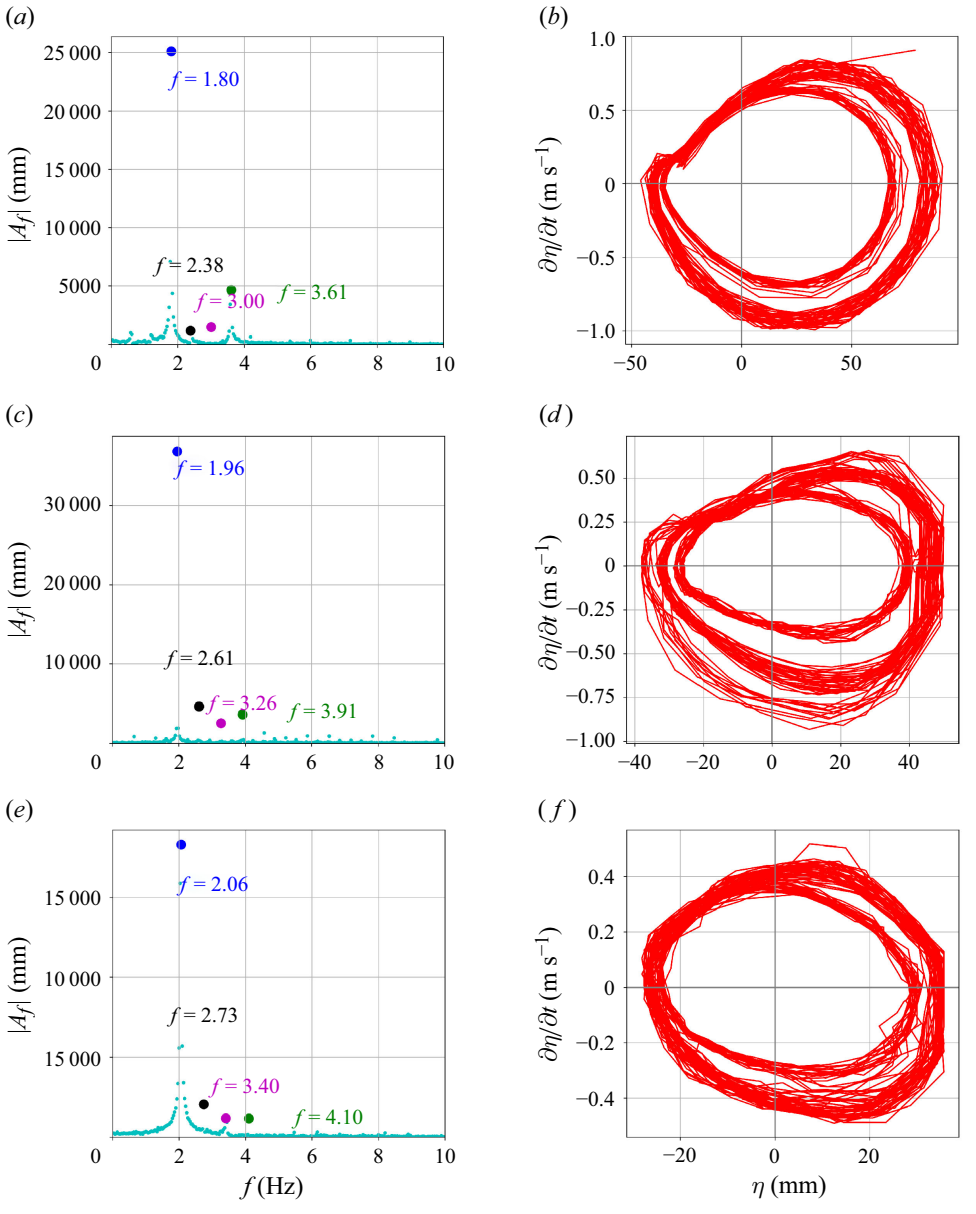

Figure 17. Frequency domain and phase plane tripling: (*a*) DFT of $h/D = 0.3$, $f = 3.595$ Hz and $\gamma = 4$ mm; (*b*) phase plane of $h/D = 0.3$, $f = 3.595$ Hz and $\gamma = 4$ mm; (*c*) DFT of $h/D = 0.5$, $f = 3.920$ Hz and $\gamma = 4$ mm; (*d*) phase plane of $h/D = 0.5$, $f = 3.920$ Hz and $\gamma = 4$ mm; (*e*) DFT of $h/D = 0.67$, $f = 4.05$ Hz and $\gamma = 2$ mm; (*f*) phase plane plot of $h/D = 0.67$, $f = 4.05$ Hz and $\gamma = 2$ mm.

Figure 17(*c*,*d*) shows the same harmonics present for an additional $h/D = 0.50$ fill level case (where $\gamma = 4$ mm). The same harmonics are present in figure 17(*e*,*f*) with a $h/D = 0.67$ fill level and a lower forcing amplitude, $\gamma = 2$.

Figures 17(*a*), 17(*c*) and 17(*e*) highlight the dominant harmonic f (blue marker), $2f/3$ (black marker), $6f/7$ (purple marker) and f (green marker). Such harmonic intervals matches that of period tripling breaking Faraday waves discovered in a rectangular tank

(Jiang, Perlin & Schultz 1998). Triple instability waves were also observed in steep waves against a vertical wall (Longuet-Higgins & Drazen 2002). This was determined to be due to nonlinear interaction between wave modes which are subsequently highlighted through the $\omega/6$ interval harmonics. These additional nonlinear interactions are not present for smaller sloshing wave amplitudes at each respective fill level see, figure 10(*c*). Figure 17(*e*) displays greater amounts of spectral leakage, this may be why $f/6$ and $f/3$ are not displayed below the dominant frequency. These are displayed on figures 17(*a*) and 17(*c*). Higher harmonics above f (i.e. $7f/6$, $4f/3$ etc.) are present in all DFT plots displayed.

To the authors knowledge this is the first time period tripling modulation has been shown for multiple fill levels. Period tripling occurs at different forcing amplitudes, the relative magnitude of the harmonics vary and the wave elevations and wave steepness at which it occurs is different for each fill level. Notably, the second dominant frequency for figures 17(*c*) and 17(*e*) occur near $2f/3$, at 2.61 Hz and 2.73 Hz, respectively. In the contrary, the second most dominant frequency occurs near, f, at 3.61 Hz in figure 17(*a*). It was reported by Jiang *et al.* (1998) that the harmonics $f/2$ and f remain strong during period tripling. In our case this appears true only in the 0.3 fill level. At 0.5 and 0.67 fill levels the $2f/3$ harmonic becomes the second dominant harmonic when period tripling occurs.

Finally, the phase plane plots displayed in figure 17 show the different mode shapes for each fill level. Figure 17(*d*) shows three distinct mode orbits. Figures 17(*b*) and 17(*f*) show two distinct orbits. Importantly, these plots display the displacement, η, showing that period tripling is present at a wave steepness of 0.32 for $h/D = 0.3$, 0.20 for $h/D = 0.5$ and 0.18 for $h/D = 0.67$. This shows that when the fill level is varied the wave height alone cannot determine if period tripling will occur. As period tripling occurs before breaking this shows that the wave height (or sloshing wave amplitude) do not provide a useful determination of wave breaking especially when multiple fill levels are considered.

5. Conclusion

A theoretical potential flow solution calculating the linear wave frequencies in a horizontal circular cylinder has been presented. The effect that different density ratios have on this wave frequency has also been solved and stability analysis has been shown when the tank is forced to oscillate vertically.

An experimental campaign exciting Faraday waves at the fundamental symmetric mode, in a quasi-two-dimensional horizontal circular tank has been performed. The parametric study has quantified the mode shapes of the free surface for multiple driving frequencies, forcing amplitudes and fill levels.

The theoretical potential flow solution has calculated the first symmetric mode frequency within the range $f/f^* = 0.949$ to 0.980 across the experimental parameter space. A soft-spring nonlinear response has been displayed where $h/D = 0.3$, 0.5 and 0.67. Higher forcing amplitudes have resulted in the experimental resonance frequency shifting away for the linear potential flow solution. At higher fill levels the experimental resonance frequency also appears to shift away from the linear potential flow solution. Sloshing wave amplitudes have been shown to be smaller near resonance for higher fluid fill levels, $h/D = 0.67$. Asymmetries between the sidewall wave height and the tank centreline are significant for lower fill levels, at higher fill levels the asymmetry between sidewalls and tank centre displacement is reduced significantly.

Period tripling, with $f/6$ harmonic intervals, has been observed for multiple fill levels in the horizontal circular tank for the first time. The harmonic $2f/3$ is the second most dominant Fourier amplitude, A_f, for the 0.5 and 0.67 fill level cases. The harmonic f is

the second most dominant amplitude for cases far from breaking. We have shown period tripling occurring at significantly smaller sloshing wave amplitudes when $h/D = 0.67$. Wave breaking cases have also been shown to occur for smaller sloshing wave amplitudes, wave steepnesses and forcing amplitudes. Additional work on the transition from non-breaking period tripling and breaking wave cases should be investigated across the fill level range tested.

This experimental study has improved our understanding of mode shapes and mode interactions for Faraday waves in a horizontal circular tank. Important differences in wave kinematics for high fill level cases have been highlighted. A large variety of sloshing wave amplitudes and near breaking wave cases have been analysed here. This will provide important benchmark test cases for non-isothermal testing to improve our understanding of the effects that varying fluid fill levels, sloshing wave amplitudes and wave breaking cases have on sloshing induced pressure drops in LH2 aircraft fuel tanks.

Funding. This work was funded by the Engineering and Physical Sciences Research Council (EPSRC) and Airbus UK (EP/W522223/1).

Declaration of interests. The authors report no conflict of interest.

References

ARNDT, T. 2012 *Sloshing of Cryogenic Liquids in a Cylindrical Tank under Normal Gravity Conditions*. Cuvillier Verlag.

ARNDT, T., DREYER, M., BEHRUZI, P. & WINTER, M. 2008 Laterally excited sloshing tests with liquid nitrogen LN2. *AIAA Paper* 2008-4551.

BARDAZZI, A., LUGNI, C., FALTINSEN, O.M., DURANTE, D. & COLAGROSSI, A. 2024 Different scenarios in sloshing flows near the critical filling depth. *J. Fluid Mech.* **984**, A73.

BELL, I.H., WRONSKI, J., QUOILIN, S. & LEMORT, V. 2014 Pure and pseudo-pure fluid thermophysical property evaluation and the open-source thermophysical property library coolprop. *Ind. Engng Chem. Res.* **53** (6), 2498–2508.

BENJAMIN, T.B. & URSELL, F.J. 1954 The stability of the plane free surface of a liquid in vertical periodic motion. *Proc. R. Soc. Lond. A* **225**, 505–515.

BREDMOSE, H., BROCCHINI, M., PEREGRINE, D.H. & THAIS, L. 2003 Experimental investigation and numerical modelling of steep forced water waves. *J. Fluid Mech.* **490**, 217–249.

BUDIANSKY, B. 1960 Sloshing of liquids in circular canals and spherical tanks. *J. Aerosp. Sci.* **27** (3), 161–173.

COLVILLE, S.W., RANSLEY, E., GAMBIOLI, F., LEE, Y.C. & GREAVES, D. 2023 Fluid response of sloshing in a horizontal cylinder due to horizontal excitation. In *International Ocean and Polar Engineering Conference*, pp. ISOPE–I–23-381. ISOPE.

COLVILLE, S.W., SCOLAN, Y.M., GAMBIOLI, F., LEE, Y.C., GREAVES, D. & RANSLEY, E. 2024 Faraday waves in a circular tank. In *39th International Workshop on Water Waves and Floating Bodies* (IWWWFB), *St Andrews, UK*, pp. 41–44.

DAS, S.P. & HOPFINGER, E.J. 2009 Mass transfer enhancement by gravity waves at a liquid–vapour interface. *Intl J. Heat Mass Transfer* **52** (5), 1400–1411.

DUDA, R.O. & HART, P.E. 1972 Use of the Hough transformation to detect lines and curves in pictures. *Commun. ACM* **15** (1), 11–15.

FALTINSEN, O.M. & TIMOKHA, A.N. 2009 *Sloshing*. Cambridge University Press.

FALTINSEN, O.M. & TIMOKHA, A.N. 2012 On sloshing modes in a circular tank. *J. Fluid Mech.* **695**, 467–477.

FRANDSEN, J. 2004 Sloshing motion in excited tanks. *J. Comput. Phys.* **196** (1), 53–87.

GAMBIOLI, F., ALEGRE, R.U., KIRBY, J., WILSON, T. & BEHRUZI, P. 2019 Experimental evaluation of fuel sloshing effects on wing dynamics. In *18th International Forum on Aeroelasticity and Structural Dynaics, IFASD*.

GRADSHTEYN, I.S. & RYZHIK, I.M. 2014 *Table of Integrals, Series, and Products*. Academic Press.

HOPFINGER, E.J. & DAS, S.P. 2009 Mass transfer enhancement by capillary waves at a liquid–vapour interface. *Exp. Fluids* **46** (4), 597–605.

IBRAHIM, R.A. 2005 *Liquid Sloshing Dynamics: Theory and Applications*. Cambridge University Press.

IBRAHIM, R.A. 2015 Recent advances in physics of fluid parametric sloshing and related problems. *J. Fluids Engng* **137** (9), 090801.

JIANG, L., PERLIN, M. & SCHULTZ, W.W. 1998 Period tripling and energy dissipation of breaking standing waves. *J. Fluid Mech.* **369**, 273–299.

JIANG, L., TING, C.-L., PERLIN, M. & SCHULTZ, W.W. 1996 Moderate and steep Faraday waves: instabilities, modulation and temporal asymmetries. *J. Fluid Mech.* **329**, 275–307.

KUMAR, K. & TUCKERMAN, L.S. 1994 Parametric instability of the interface between two fluids. *J. Fluid Mech.* **279**, 49–68.

LACAPERE, J., VIEILLE, B. & LEGRAND, B. 2009 Experimental and numerical results of sloshing with cryogenic fluids. *Prog. Propul. Phys.* **1**, 267–278.

LONGUET-HIGGINS, M.S. & DRAZEN, D.A. 2002 On steep gravity waves meeting a vertical wall: a triple instability. *J. Fluid Mech.* **466**, 305–318.

LUDWIG, C., DREYER, M.E. & HOPFINGER, E.J. 2013 Pressure variations in a cryogenic liquid storage tank subjected to periodic excitations. *Intl J. Heat Mass Transfer* **66**, 223–234.

MACCARTY, J.L. & STEPHENS, D.G. 1960 *Investigation of the Natural Frequencies of Fluids in Spherical and Cylindrical Tanks*. National Aeronautics and Space Administration.

MARAGOS, P. & SCHAFER, R.W. 1990 Morphological systems for multidimensional signal processing. *Proc. IEEE* **78** (4), 690–710.

MARQUES, P.A., SIMONINI, A., PEVERONI, L. & MENDEZ, M.A. 2023 Experimental analysis of heat and mass transfer in non-isothermal sloshing using a model-based inverse method. *Appl. Therm. Engng* **231**, 120871.

MCIVER, P. 1989 Sloshing frequencies for cylindrical and spherical containers filled to an arbitrary depth. *J. Fluid Mech.* **201** (1), 243–257.

MILES, J.W. 1984 Resonantly forced surface waves in a circular cylinder. *J. Fluid Mech.* **149** (1), 15–31.

MORAN, M., MCNELIS, N., KUDLAC, M., HABERBUSCH, M. & SATORNINO, G. 1994 Experimental results of hydrogen slosh in a 62 cubic foot (1750 liter) tank. *AIAA Paper* 94-3259.

NYSTRÖM, E.J. 1930 Über die praktische auflösung von integralgleichungen mit anwendungen auf randwertaufgaben. *Acta Mathematica* **54** (1), 185–204.

ONORATO, G., PROESMANS, P. & HOOGREEF, M.F.M. 2022 Assessment of hydrogen transport aircraft: effects of fuel tank integration. *CEAS Aeronaut. J.* **13** (4), 813–845.

RAYLEIGH1882 Investigation of the character of the equilibrium of an incompressible heavy fluid of variable density. *Proc. Lond. Math. Soc.* **14**, 170–177.

RAJCHENBACH, J. & CLAMOND, D. 2015 Faraday waves: their dispersion relation, nature of bifurcation and wavenumber selection revisited. *J. Fluid Mech.* **777**, R2.

SALTARI, F., PIZZOLI, M., MIGLIORINI, M.T., BINNI, A., COPPOTELLI, G., MASTRODDI, F., PAGLIAROLI, T., DEL DUCHETTO, F., GAMBIOLI, F., ABARCA, R. & SCHEUFLER, H. 2024 Experimental investigations on the sloshing-induced pressure drop in tanks for hydrogen-powered aircraft. *AIAA Paper* 2024-2158.

SCHULTZ, W.W., VANDEN-BROECK, J.-M., JIANG, L. & PERLIN, M. 1998 Highly nonlinear standing water waves with small capillary effect. *J. Fluid Mech.* **369**, 253–272.

SCOLAN, Y.-M. 2015 Some aspects of the eigenfrequency computation in a two-dimensional tank filled with two non miscible fluids. In *30th International Workshop on Water Waves and Floating Bodies* (IWWWFB), *Bristol, UK*, pp. 189–192.

SILBERHORN, D., ATANASOV, G., WALTHER, J.-N. & ZILL, T. 2019 Assessment of hydrogen fuel tank integration at aircraft level. In *Proceedings of the Deutscher Luft-und Raumfahrtkongress*, pp. 1–14. Deutsche Gesellschaft für Luft- und Raumfahrt.

WRIGHT, J., YON, S. & POZRIKIDIS, C. 2000 Numerical studies of two-dimensional Faraday oscillations of inviscid fluids. *J. Fluid Mech.* **402**, 1–32.